JOURNAL OF SPACECRAFT AND ROCKETS
Vol. 30, No. 6, November–December 1993

Unsteady Flow Separation on Slender Bodies at High Angles of Attack

L. E. Ericsson*
Lockheed Missiles and Space Company, Inc., Sunnyvale, California 94040

Experimental results for unsteady flow separation on slender bodies at high angles of attack have been analyzed. Flow hypotheses are presented that can explain the seemingly contradictory experimental results. The analysis should contribute significantly toward providing the understanding of the high-alpha unsteady fluid mechanics needed before the occurrence of asymmetric forebody flow separation with associated asymmetric vortices can be predicted and reliable means of control can be developed for maneuvering aircraft and missiles.

Nomenclature

c = reference length, D except $c = D_B$ for cones and ogives
D = cylinder diameter
D_B = base diameter
L = total body length
L_N = nose length
M = Mach number
n = rotation or spin rate
q_∞ = dynamic pressure, $\rho_\infty U_\infty^2/2$
R = nose radius (see Fig. 1)
Re = Reynolds number, usually $Re = U_\infty c/\nu_\infty$
t = time
U_∞ = freestream velocity
U_V = mean vortex convection velocity
x = axial distance from nose (see Fig. 1)
x_{AV} = location of starting vortex asymmetry
Y = side force, coefficient $C_Y = Y/q_\infty$; $c_y = \delta C_Y/\partial\xi$
α = angle of attack
$\dot{\alpha}$ = $\partial\alpha/\partial t$
$\tilde{\alpha}$ = effective angle of attack, Eq. (1)
$\bar{\dot{\alpha}}$ = normalized pitch rate, $\dot{\alpha}x_{cg}/U_\infty$
θ_A = apex half-angle
ν = kinematic viscosity of air
ξ = dimensionless x coordinate, x/c
ρ = density of air
ϕ = roll angle

Subscripts

A = apex
AV = asymmetric vortices
B = base
cg = center of gravity
V = vortex
∞ = freestream conditions

Introduction

HIGH performance aircraft and missiles are required to perform rapid maneuvers at high angles of attack[1-3] where the vehicles are subject to unsteady separated flowfields that generate highly nonlinear aerodynamics with strong coupling between longitudinal and lateral degrees of freedom.[4,5] This cross coupling exists even at zero angle of sideslip for

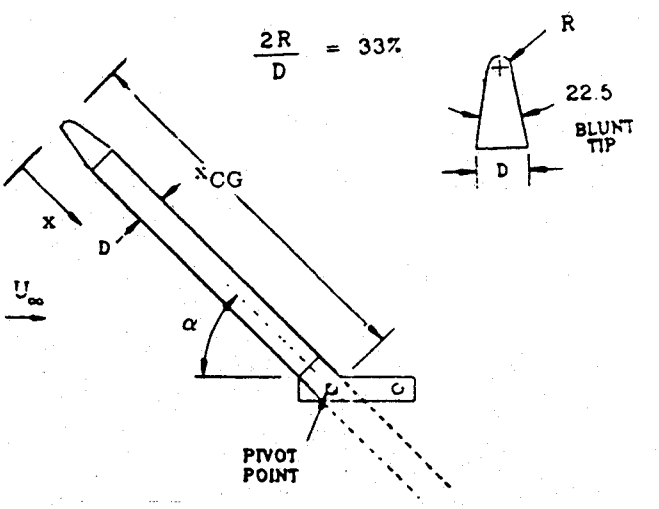

Fig. 1 Tested blunted cone-cylinder.[9]

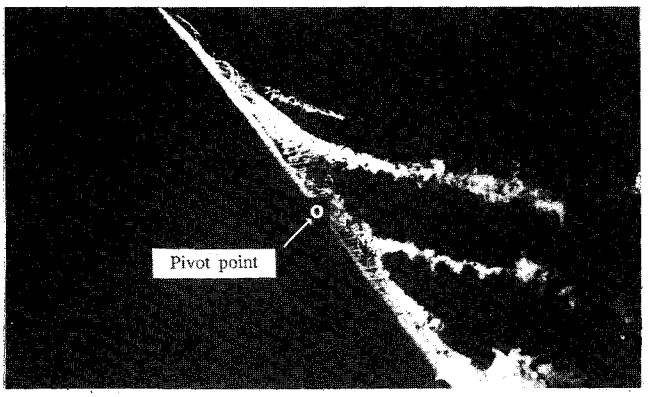

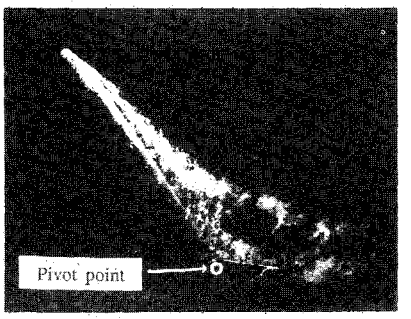

Fig. 2 Effect of afterbody on forebody vortices at $\alpha = 55$ deg for the reduced pitch-up rate $\bar{\dot{\alpha}} = 0.175$ (Ref. 9).

Received Dec. 11, 1990; revision received Jan. 23, 1993; accepted for publication Jan. 23, 1993.

*Retired; presently Engineering Consultant. Fellow AIAA.

high angles of attack where the flow separation becomes asymmetric on a slender forebody.[6] This can result in dynamic instability of aircraft and missiles through dynamic cross-coupling effects.[7]

Because of the strong coupling existing between vehicle motion and flow separation through so-called moving wall effects,[8] a thorough understanding of the high-alpha unsteady fluid mechanics is needed before the performance and stability

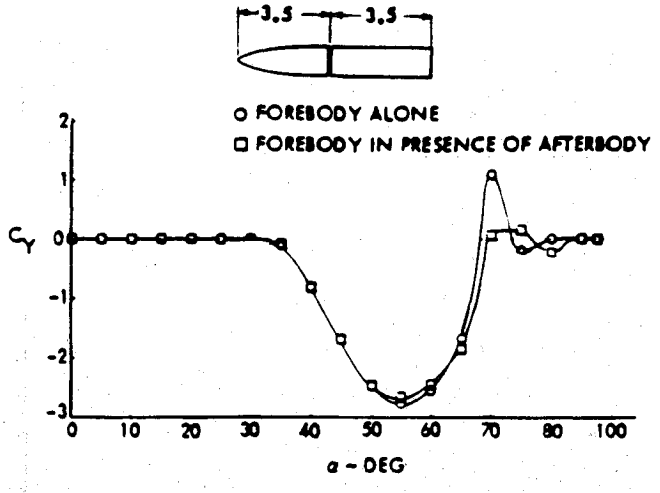

Fig. 3 Effect of cylindrical afterbody on forebody side force.[10]

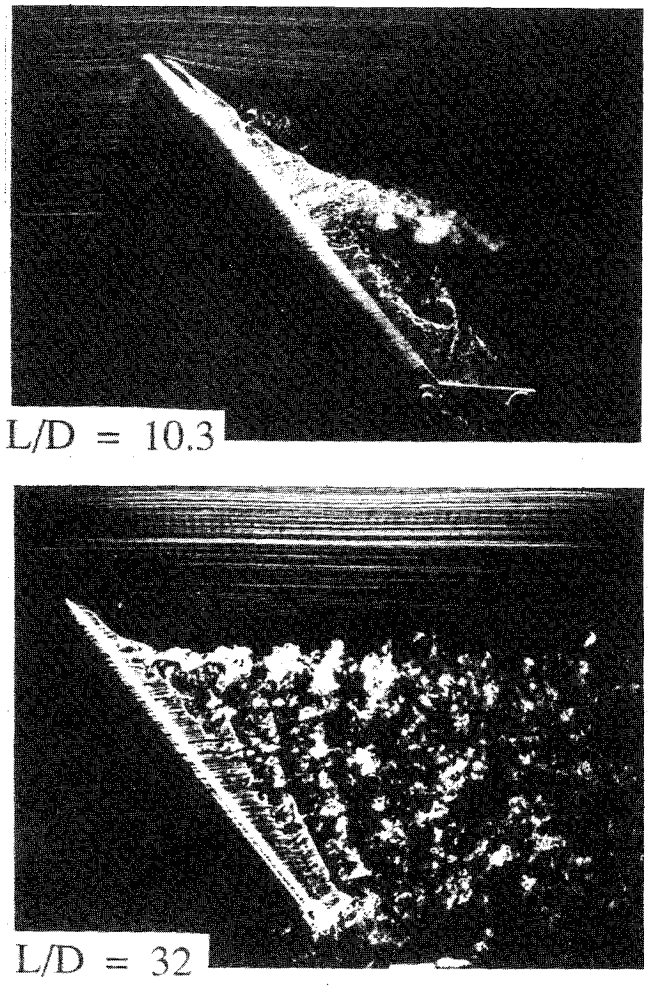

Fig. 4 Vortex patterns at $\alpha = 50$ deg on two slender bodies of $L/D = 10.3$ and 32 at steady flow conditions.[9]

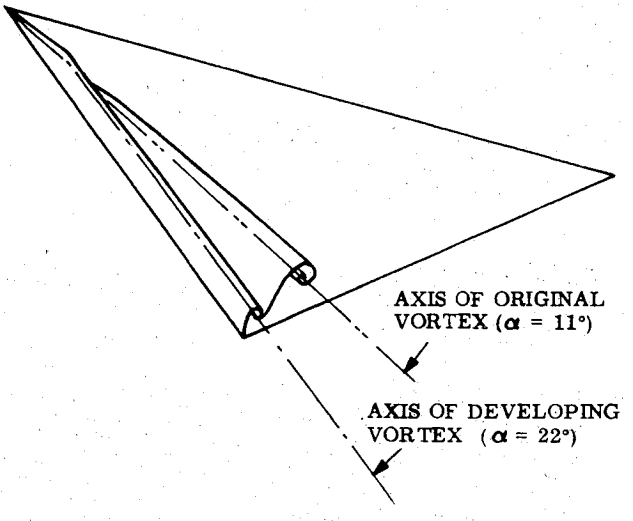

Fig. 5 Leading-edge vortex development on delta wing for a stepwise change of angle of attack.[12]

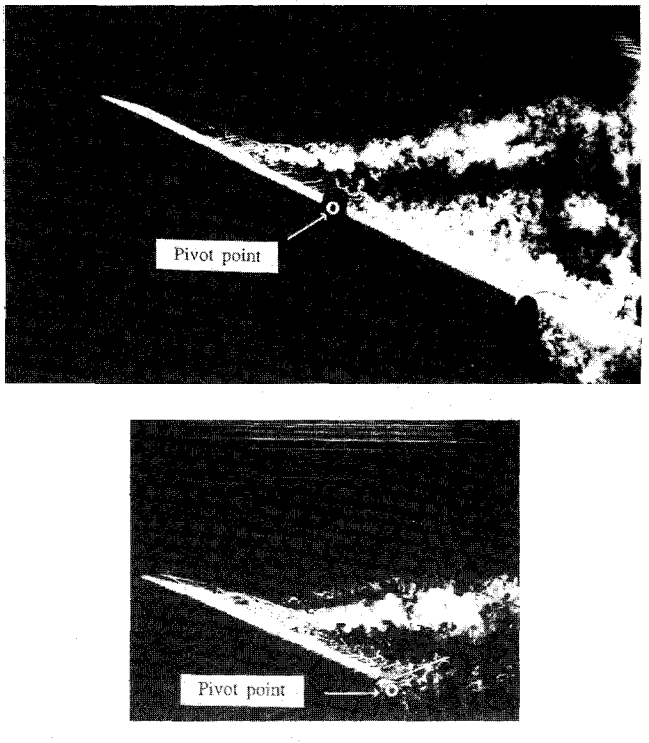

Fig. 6 Effect of afterbody on forebody vortices at $\alpha = 25$ deg for the pitch-down rate $\tilde{\alpha} = -0.175$ (Ref. 9).

characteristics of manuevering aircraft and missiles can be predicted and needed means of control can be developed. The present paper analyzes available experimental results in an effort to contribute toward the needed better understanding of the high-alpha aerodynamics of maneuvering vehicles.

Discussion

A blunted cone-cylinder model[9] (Fig. 1) has been tested in laminar flow at large pitch rates, $-0.35 \leq \tilde{\alpha} \leq 0.35$. Figure 2 shows that the addition of a cylindrical section aft of the rotation center has no effect on the asymmetric vortex geometry on the forebody. This is in agreement with static balance measurements for an ogive-cylinder body[10] (Fig. 3) but is in apparent conflict with the experimental results[9] in Fig. 4, which show that the presence of a longer afterbody has a

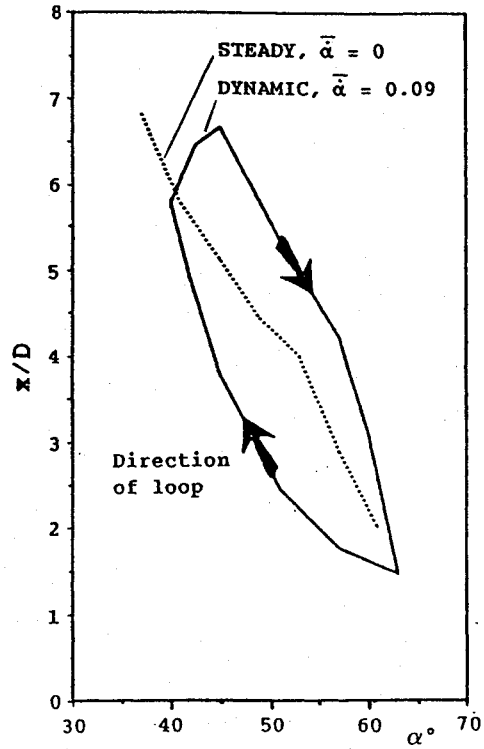

Fig. 7 Hysteresis loops for cone-cylinder body of L/D = 10.3 (Ref. 9).

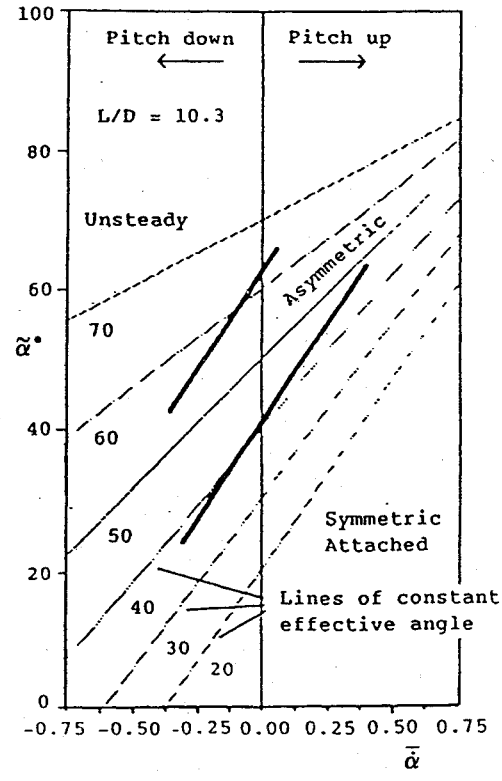

Fig. 8 Effective angle of attack as a function of $\bar{\dot{\alpha}}$ for the L/D = 10.3 body.[9]

profound influence on the overall vortex flow pattern. What is the explanation?

On a pointed ogive cylinder, asymmetric vortex shedding should start at[6] $\alpha_{AV} = 2\theta_A = 2 \tan^{-1} \{l_N/c/[(l_N/c)^2 - 0.25]\}$, which gives $\theta_{AV} = 32.5$ deg for $l_N/d = 3.5$, in agreement with the experimental results[10] in Fig. 3. However, for the blunted cone-cylinder body in Fig. 1, asymmetric flow separation and associated vortex shedding occurs first on the aftbody, at $\alpha_{AV} \approx 4.2\, D/L$ according to the experiment.[11] That is, α_{AV} = 23 and 7.5 deg for L/D = 10.3 and 32, respectively, in Fig. 4. As a consequence, the unsteady vortex shedding, starting at the base[6,11] has had three times as large an α/α_{AV} range to develop and move toward the nose for L/D = 32 as for L/D = 10.3; for the same α, α = 50 deg in Fig. 4. That explains the absence of unsteady vortex shedding on the aftbody for L/D = 10.3 and the dominant presence of it for L/D = 32. Why, then, is not this dominant unsteady vortex shedding not observed on the long afterbody in Fig. 2?

Analysis

The results in Fig. 2 are the "frozen," instantaneous pictures, taken at α = 55 deg, when the angle of attack is increased at a certain rate. The instantaneous angle of attack at the apex is

$$\tilde{\alpha} = \alpha - \dot{\alpha} x_{cg}/U_\infty \tag{1}$$

As in the case of leading-edge vortices[12] (Fig. 5), the vortex at a downstream station x reacts to the changed flow conditions at the apex at a time Δt later, where $\Delta t = x/U_V$. The convection velocity U_V is approximately equal to the free-stream velocity.[12] Thus, the effective angle of attack $\tilde{\alpha}(x, t)$, determining the vortex characteristics at station x, is

$$\tilde{\alpha}(x, t) = \tilde{\alpha}(0, t - \Delta t) \tag{2}$$

with $\Delta t \approx x/U_\infty$.

For small reduced frequencies $\bar{\dot{\alpha}}^2 << 1$, and Eq. (2) can be written

$$\tilde{\alpha}(x, t) \approx \tilde{\alpha}_A(t) - \Delta t\, \partial\alpha/\partial t = \tilde{\alpha}_A - \dot{\alpha} x/U_\infty \tag{3}$$

Combining Eqs. (1) and (3) gives

$$\tilde{\alpha}(x, t) = \alpha - \bar{\dot{\alpha}}\,(1 + x/x_{cg}) \tag{4}$$

According to the results in Fig. 2, $x_{AV}/D \approx 4$. Thus, for $\bar{\dot{\alpha}} = 0.175$ and x_{cg}/D = 10.3, Eq. (4) gives $\tilde{\alpha}(x, t) = \alpha - 13.9$ deg = 41.1 deg. That is, even with the added cylindrical afterbody, the unsteady Karman-type vortex shedding probably did not have a large enough α/α_{AV} range to develop on the forebody. This explains the similarity between the forebody vortex geometry in Fig. 2 and the static vortex formation for L/D = 10.3 in Fig. 4. For the pitch-down case at α = 25 deg in Fig. 6, $\tilde{\alpha}(x, t) = \alpha + 13.9$ deg = 38.9 deg, compared to $\tilde{\alpha}(x, t)$ = 41.1 deg in Fig. 2, explaining the similarity between the forebody vortex geometries in Figs. 2 and 6.

This difference in $\tilde{\alpha}(x, t)$ between upstroke and downstroke causes the experimentally observed hysteresis[9] shown in Fig. 7. With $\bar{\dot{\alpha}} = 0.09$, Eq. (4) gives a difference $\Delta\tilde{\alpha}$ = 14.4 deg between upstroke and downstroke for $x_{AV}/D = 4$ and L/D = 10.3. This is in good agreement with the experimental results in Fig. 7. If the time-lag effect had been included in the computation of the "effective angle of attack" in Ref. 9, the predicted $\bar{\dot{\alpha}}$ slope would have increased in magnitude by 40%, bringing it into good agreement with the experimentally determined boundaries for symmetric and asymmetric vortex shedding in Fig. 8.

On the 15.5 caliber body with a 2.5 caliber ogival nose, tested by Fidler[13] (Fig. 9), asymmetric vortex shedding should start on the afterbody when α = 15.6 deg and should not occur on the nose[6] until α = 45 deg. Thus, the measured effect of the various rotating nose tips at 22.5 deg < α < 45 deg (Figs. 10–12) occurred through changes of the symmetric flow separation on the nose. When the angle of attack becomes substan-

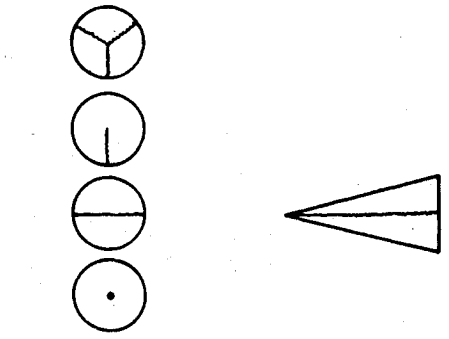

Tip grit patterns.

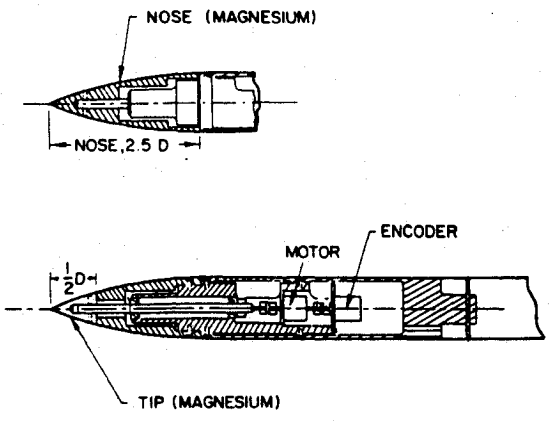

Spinning nose and tip models.

Fig. 9 Tested pointed ogive-cylinder geometry with various spinning nose tips.[13]

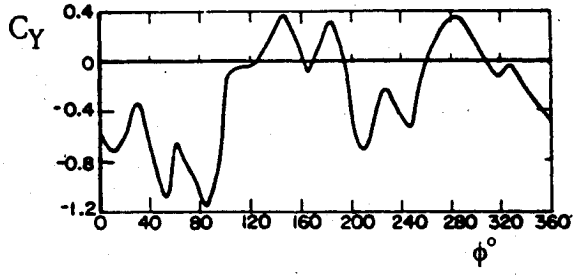

Tip with three grit strips, +2 rps

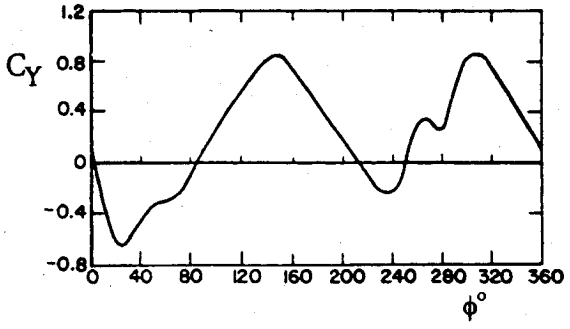

Tip with three grit strips, +5 rps

Fig. 10 Effect of roll angle and rotation rate on measured side force characteristics at $\alpha = 30$ deg and $M_\infty = 0.6$ for nose tip with three grit strips spinning at moderate rates.[13]

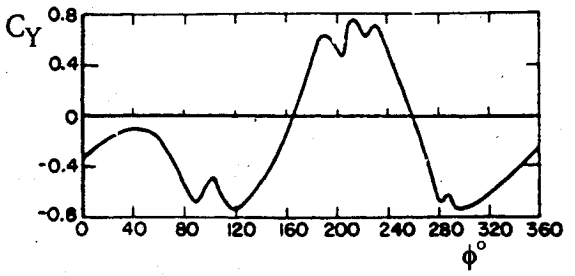

Tip with three grit strips, +10 rps

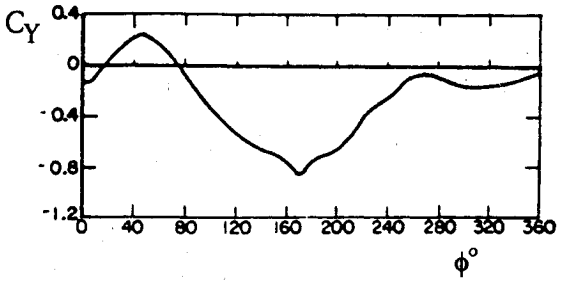

Tip with three grit strips, +20 rps

Fig. 11 Effect of roll angle and rotation rate on measured side force characteristics at $\alpha = 30$ deg and $M_\infty = 0.6$ for nose tip with three grit strips spinning at high rates.[13]

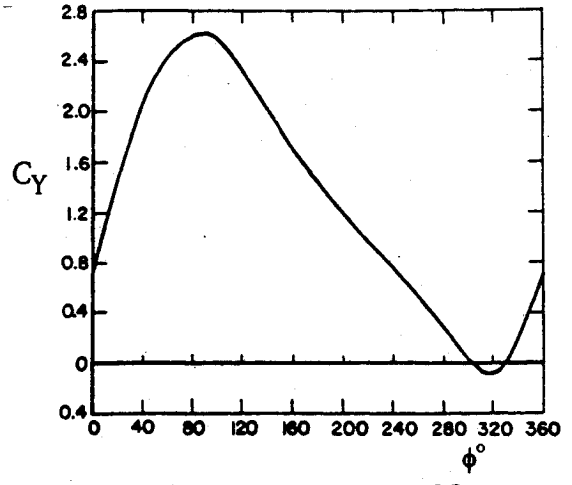

Tip with one grit strip, +20 rps

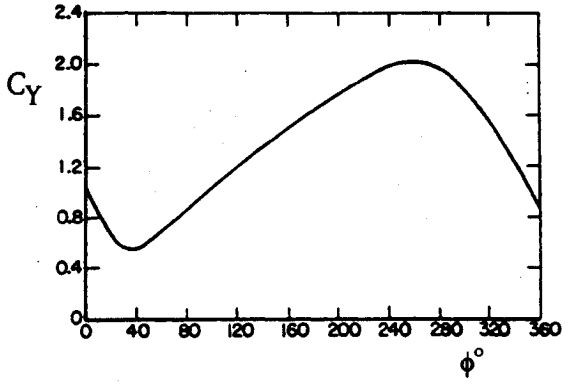

Tip with one grit strip, -20 rps

Fig. 12 Effect of roll angle and rotation rate on measured side force at $\alpha = 45$ deg and $M_\infty = 0.25$ for nose tip with one grit strip spinning at $\pm$ 20 rps.[13]

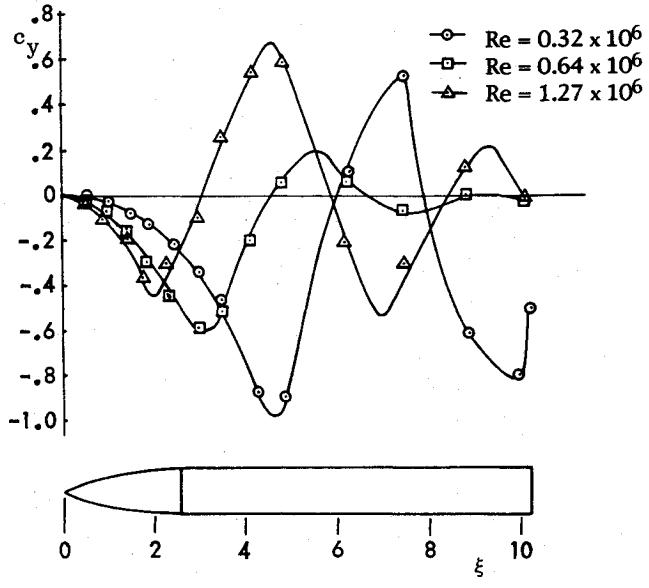

Fig. 13 Effect of Reynolds number on side force distribution over pointed ogive cylinder at $\alpha = 50$ deg and $M_\infty = 0.4$ (Ref. 14).

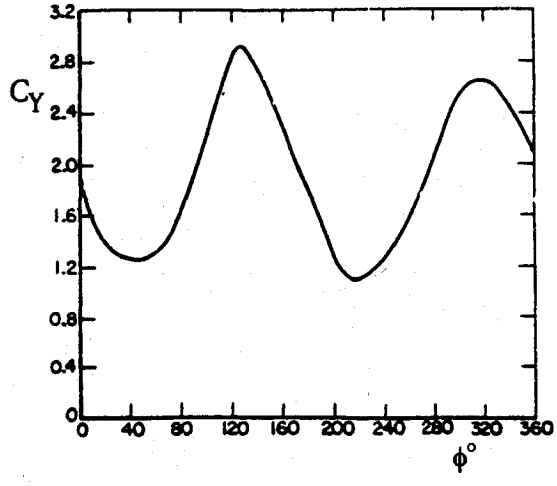

Tip with two grit strips, -10 rps

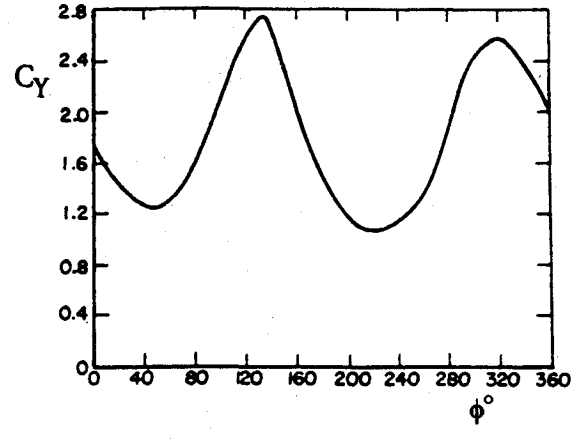

Tip with two grit strips, +10 rps

Fig. 14 Effect of roll angle and rotation rate on side force at $\alpha = 50$ deg and $M_\infty = 0.25$ for nose tip with two grit strips spinning at ± 10 rps.[13]

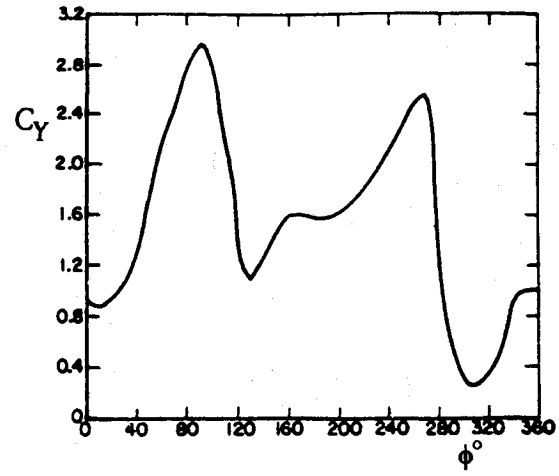

Nose with three tape strips, +10 rps

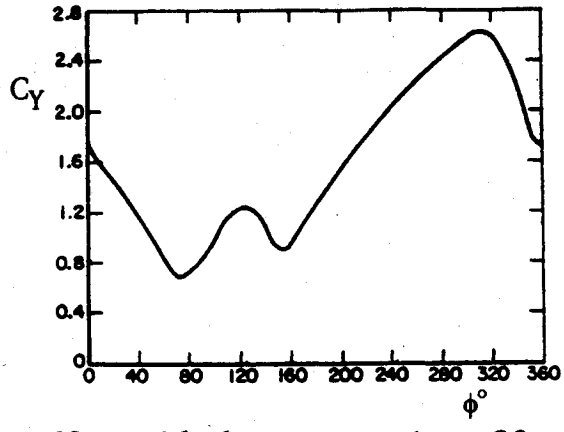

Nose with three tape strips, +20 rps

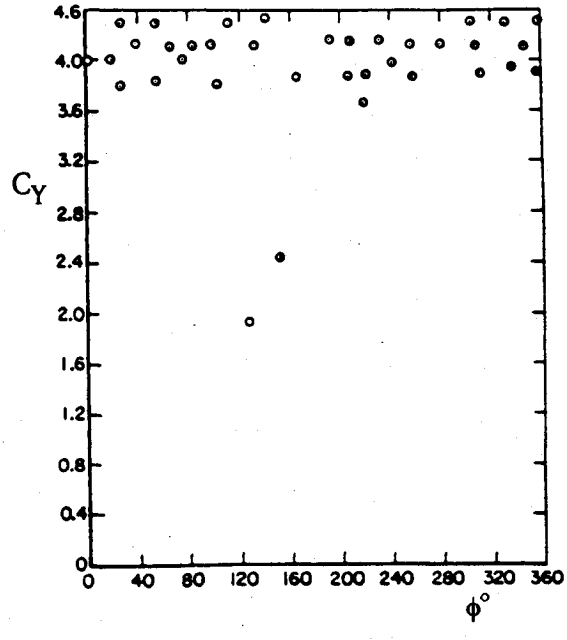

Nose with three tape strips, +50 rps

Fig. 15 Effect of roll angle and rotation rate on measured side force at $\alpha = 50$ deg and $M_\infty = 0.25$ for nose tip with three tape strips.[13]

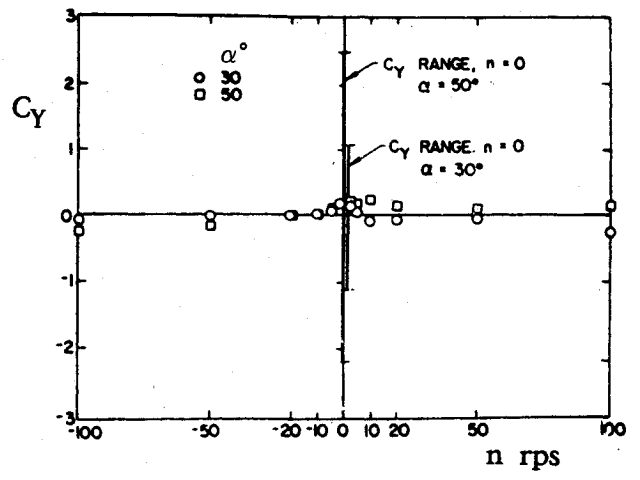

Tip with three grit strips

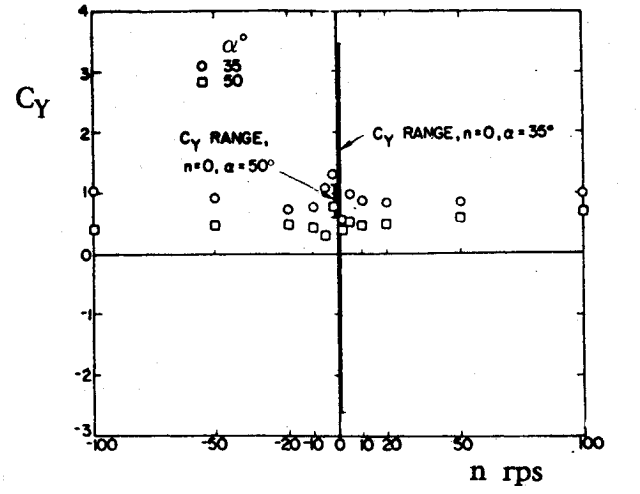

Tip with two grit strips

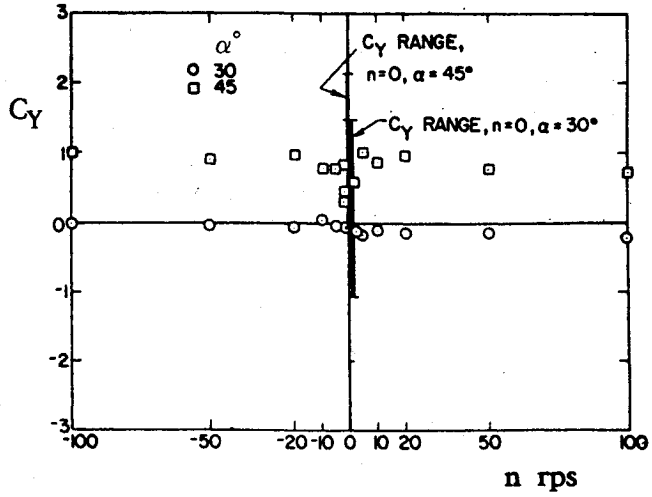

Tip with one grit strip

Fig. 16 Effect of rotation rate and number of grit strips on the mean side force measured by a static balance at $M_\infty = 0.25$ and various angles of attack.[13]

tially larger than α_{AV} ($\alpha_{AV} \approx$ 16 deg for the aftbody vortices on the tested geometry, Fig. 9), the asymmetric flow separation becomes of the multicell type[6] with associated changes of the local side force distribution[14] (Fig. 13). Thus, at $\alpha = 30$ deg (Figs. 10 and 11), two side-force cells may exist on the aftbody, giving close to zero net side force. In this case, therefore, the distortion of the symmetric flow separation on the nose through the rotating nose tip could dominate to produce the experimentally observed sign changes of the total side force. At $\alpha = 45$ deg, however, more than two side-force cells would presumably exist on the aftbody, producing a significant net side force. This explains the data trend in Fig. 12, which shows that no consistent sign change of the side force occurred in spite of the fact that the nose tip induced side-force variation is much larger than at $\alpha = 30$ deg (compare Fig. 12 with Figs. 10 and 11).

At $\alpha > 45$ deg, e.g., at $\alpha = 50$ deg as in Figs. 14 and 15, the nose generates a significant side force, even in the absence of a spinning nose tip. Based upon static experimental results one expects the nose-generated flow asymmetry and associated asymmetric vortices to dominate the time-averaged afterbody flow asymmetry.[6] Actually, a flow visualization movie of the flow for a spinning nose tip shows the asymmetric flowfield over the aftbody to have a variation tied to the nose tip rotation.[15] The results in Figs. 14 and 15 show that the rotation rate of the nose tip had to be increased to 50 rps before the moving wall effect[8] could overpower the microasymmetry effect of the three tape strips. When this happens, the magnitude of the side force is roughly doubled, as can be seen by comparing the results in Fig. 15c with those in Figs. 14a and b and 15a and b. The two low data points in Fig. 15c, for which roll angle the moving wall effect apparently could not overpower the nose-microasymmetry effect, also illustrate this large effect of the spinning nose tip, when compared to the main data trend.

When the measured side force is time averaged, using a standard static force balance, the spinning nose tip gives, as expected, a C_Y value that falls close to the center of the C_Y range measured in static tests for zero spin rate (Fig. 16). This trend also holds for the smooth nose tip at $\alpha = 58$ deg, but not at $\alpha = 55$ deg (Fig. 17). What can be the cause of these widely different flow characteristics?

As $\alpha_{AV} \approx 45$ deg for the 2.5 caliber pointed, ogival nose,[6] at $\alpha = 55$ deg the nose probably dominates the asymmetric force generation over the total vehicle. This would be in agreement with the data trend[10] in Fig. 3. Thus, changing the direction of the spinning nose tip flips the asymmetry between the two extreme values (Fig. 17). Why does this not also occur at $\alpha =$ 58 deg? For the cylindrical afterbody with $\alpha_{AV} \approx$ 16 deg, Karman vortex shedding will occur over a larger and larger part of the aftbody when the angle of attack is increased. This oscillatory side-force generation on the aftbody competes with

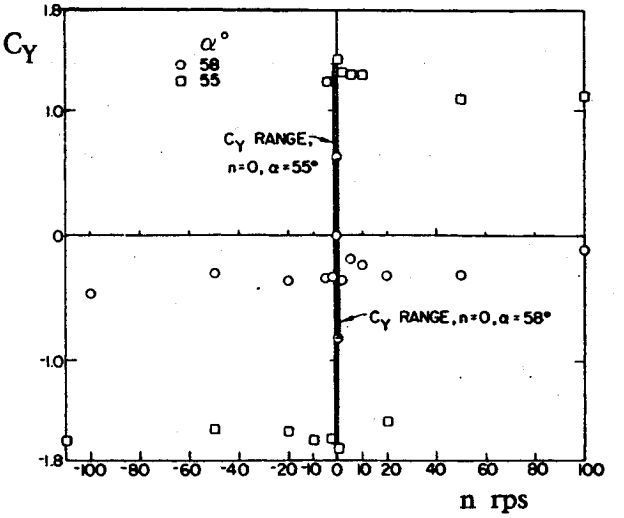

Fig. 17 Effect of rotation rate for a smooth nose tip on the mean side force measured by a static balance at $M_\infty = 0.6$ (Ref. 13).

the side-force modulation effect of the rotating nose tip on the forebody. As the region of Karman vortex shedding approaches the nose with increasing α, its effectiveness in generating lateral support oscillations[16] is increased. The magnitude of the side force on the nose passes its peak at same angle of attack (Fig. 3). Thus, at a certain higher angle of attack one can expect the oscillatory yawing moment, generated by Karman vortex shedding, to start dominating over the nose-induced yawing moment, allowing lateral support oscillations to occur. This has been observed in "static" tests, as is discussed in detail in Ref. 16. Thus, at $\alpha = 58$ deg in Fidler's test,[13] lateral support oscillations could have generated the observed near zero time average of the side force (Fig. 17).

Conclusions

An analysis of available experimental results for unsteady flow separation on slender bodies at high angles of attack has provided phenomenological explanations to many of the observed data trends. However, because of the complexity of the unsteady flow separation, including test-peculiar flow phenomena, much research is needed before the unsteady flow separation on maneuvering aircraft and missiles can be predicted with the reliability needed for preliminary design.

Acknowledgment

The paper is based upon results developed under contract to Flight Dynamics Laboratory/FIGC, Wright Patterson Air Force Base, Contract F33615-87-C-3607, monitored by W. B. Blake.

References

[1]Herbst, W. B., "Future Fighter Technologies," *Journal of Aircraft*, Vol. 17, No. 8, 1980, pp. 561–566.

[2]Herbst, W. B., "Supermaneuverability," *Proceedings of Airforce Office of Scientific Research-FJSRL—University of Colorado Workshop on Unsteady Separated Flow*, U.S.A.F. Academy, Colorado Springs, CO, Aug. 1983, pp. 1–9.

[3]Ashley, H., "On the Feasibility of Low-Speed Aircraft Maneuvers Involving Extreme Angles of Attack," *Journal of Fluids and Structures*, Vol. 1, July 1987, pp. 319–335.

[4]Orlik-Rückemann, K. J., "Aerodynamic Aspects of Aircraft Dynamics at High Angles of Attack," *Journal of Aircraft*, Vol. 20, No. 9, 1983, pp. 737–752.

[5]Orlik-Rückemann, K. J., "Aerodynamic Coupling Between Lateral and Longitudinal Degrees of Freedom," *AIAA Journal*, Vol. 15, No. 12, 1977, pp. 1792–1799.

[6]Ericsson, L. E., and Reding, J. P., "Asymmetric Vortex Shedding from Bodies of Revolution," *Tactical Missile Aerodynamics*, edited by M. J. Hemsch and J. N. Nielsen, Vol. 104, Progress in Astronautics and Aeronautics, AIAA, New York, 1986, Chap. VII, pp. 243–296.

[7]Ericsson, L. E., "Wing Rock Generated by Forebody Vortices," *Journal of Aircraft*, Vol. 26, No. 2, 1989, pp. 110–116.

[8]Ericsson, L. E., "Moving Wall Effects in Unsteady Flow," *Journal of Aircraft*, Vol. 25, No. 11, 1988, pp. 977–990.

[9]Montevidas, R. E., Reisenthel, P., and Nagib, H. N., "The Scaling and Control of Vortex Geometry Behind Pitching Cylinders," AIAA Paper 89-1003, March 1989.

[10]Keener, E. R., Chapman, G. T., and Kruse, R. L., "Effects of Mach Number and Afterbody Length on Onset of Asymmetric Forces on Bodies at Zero Sideslip and High Angles of Attack," AIAA Paper 76-66, Jan. 1976.

[11]Fiechter, M., "Über Wirbelsysteme an schlanken Rotationskörpern und ihren Einfluss auf die aerodynamische Beiwerte," Bericht 10/66, Deutsch-Französisches Forchungsinstitut, Saint Louis, France, Dec. 1966.

[12]Lambourne, N. C., Bryer, D. W., and Maybrey, J. F. M., "The Behavior of the Leading-Edge Vortices over a Delta Wing Following a Sudden Change of Incidence," Aeronautical Research Council, R&M 3645, England, UK, March 1969.

[13]Fidler, J. E., "Active Control of Asymmetric Vortex Effects," *Journal of Aircraft*, Vol. 18, No. 4, 1981, pp. 267–272.

[14]Dahlem, V., Flaherty, J., Sherida, D. E., and Przirembel, C.E.G., "High Angle of Attack Missile Aerodynamics at Mach Numbers 0.3 to 1.5," Air Force Wright Aeronautical Lab., TR-80-3070, WL, Wright Patterson AFB, OH, Nov. 1980.

[15]Fidler, J. E., private communication of flow visualization results, Nov. 1989.

[16]Ericsson, L. E., "Lateral Oscillations of Sting-Mounted Models at High Alpha," *Journal of Spacecraft and Rockets*, Vol. 27, No. 5, 1990, pp. 508–513.